Multifunctionality of Layered Materials

Septiany, Liany

DOI:
10.33612/diss.182500502

Chapter 5

Magnetocaloric Effect and Critical Behaviour in Arylamine-based Copper Chloride Organic-Inorganic Perovskites

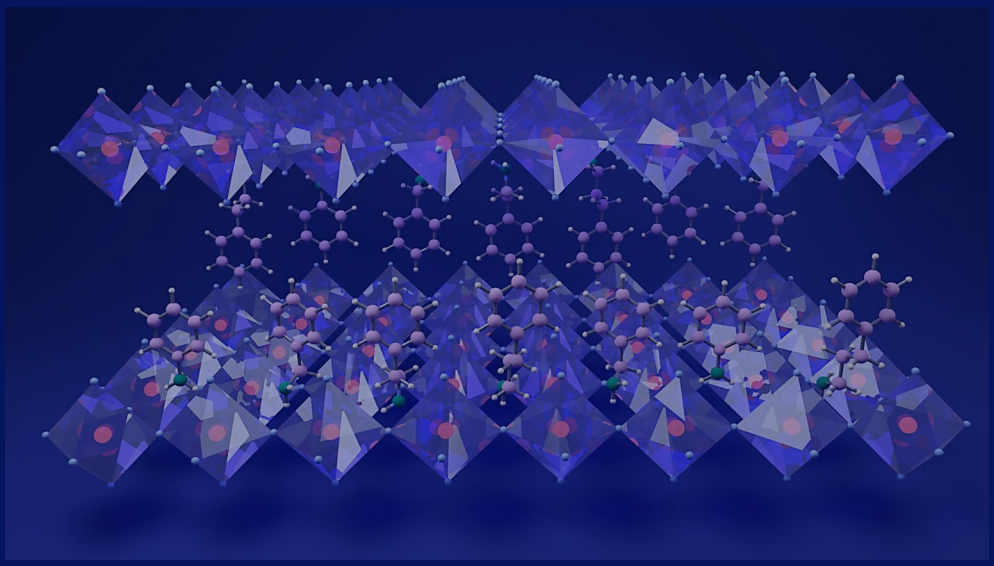

L. Septiany, G.R. Blake
Magnetocaloric Effect and Critical Behaviour in Arylamine-based Copper Chloride.
Journal of Magnetism and Magnetic Materials. **2021**. In Press.

Abstract

Layered organic-inorganic hybrid perovskites have been the focus of much research regarding their optoelectronic and multiferroic properties. Here, we demonstrate the presence of a large magnetocaloric effect in the ferromagnetic layered perovskite phenylmethylammonium copper chloride ($(PMA)_2CuCl_4$) below the Curie temperature of ~9.5 K. We measure a magnetic entropy change ranging from 0.88 J/kg.K to 2.98 J/kg.K in applied fields of 10 kOe and 70 kOe, respectively. We also study the nature of the magnetic phase transition using critical isotherm analysis. The critical exponents are consistent with the 2D-XY spin model.

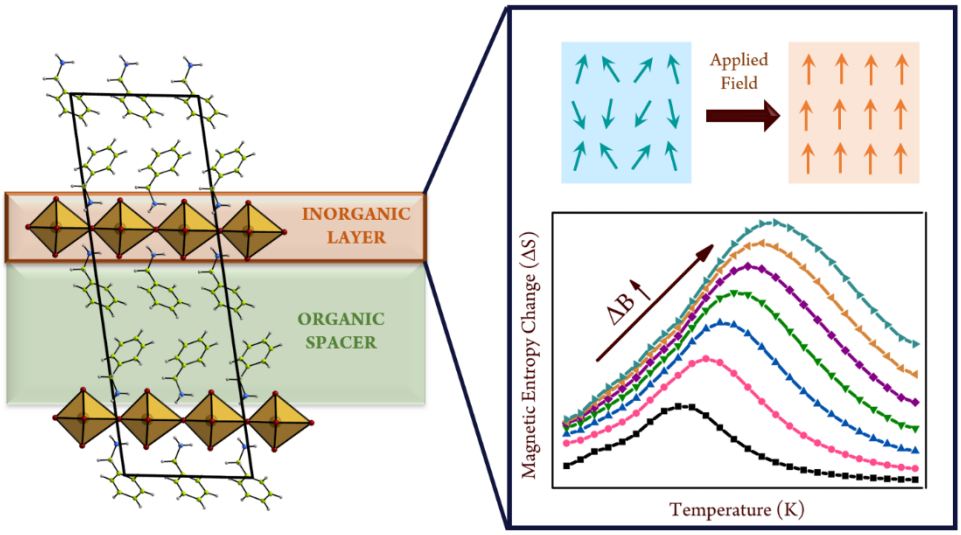

5.1 Introduction

Layered organic-inorganic hybrid perovskites have gained much attention over the past decade due to their tunable multifunctional properties applied to areas of research such as optoelectronics, ferroelectricity, and two-dimensional (2D) (anti)ferromagnetism [1–7]. Compared to their 3D counterparts, 2D perovskites have more structural freedom regarding the organic component of the material. Whereas only a limited set of small organic cations can be incorporated in 3D hybrid perovskites, much longer cations can be used in 2D perovskites [8–15]. This leads to an advantage of 2D perovskites that they are more stable under standard environmental conditions, mainly due to the hydrophobicity of the larger organic cations [16].

Recently, a large magnetic entropy change was observed in the 2D perovskites $(MA)_2CuCl_4$ [17], $(C_{12}H_{25}NH_3)_2CuCl_4$ [18], and $(C_2H_5NH_3)_2CoCl_4$ [19], with a magnitude comparable to that in all-inorganic compounds. Large magnetic entropy changes are related to the magnetocaloric effect which is important in magnetic refrigeration applications. The magnetocaloric effect (MCE) refers to a thermodynamic phenomenon where applying an external magnetic field under adiabatic conditions results in a temperature change in a magnetic material [20–24]. The MCE is an intrinsic property of a material and the largest effect is usually found close to magnetic phase transitions, particularly when associated with strong spin-lattice coupling at a paramagnetic to ferromagnetic phase transition. The compounds referred to above contain organic cations with linear alkyl chains, but a large number of 2D perovskites containing arylamine-based cations are also known. Many of these adopt polar crystal structures, leading to ferroelectric [25] and multiferroic[26] properties as well as 2D magnetism[27,28]. Here we show that the arylamine-based perovskite $(C_6H_5CH_2NH_3)_2CuCl_4$, referred to hereafter as $(PMA)_2CuCl_4$, also exhibits a large magnetocaloric effect. The ferromagnetic properties of $CuCl_4$-based perovskites were first investigated in the 1970s using magnetization, electron paramagnetic resonance (EPR), and nuclear magnetic resonance (NMR) measurements [28–30]. $(PMA)_2CuCl_4$ was identified as a quasi-2D XY ferromagnet with T_c ~8K. The J'/J ratio was calculated to be $\sim 10^{-5}$, where J is the exchange constant between neighbouring Cu^{2+} cations within a magnetic layer, and J' is the exchange constant between Cu^{2+} cations in adjacent layers, separated by bilayers of PMA cations.

Here we demonstrate that the T_c of $(PMA)_2CuCl_4$ changes significantly with external field strength. A large magnetic entropy change is observed from the field dependence of the magnetization, ranging from 0.88 J/Kg.K to 2.98 J/Kg.K in applied fields of 10kOe and 70kOe, respectively. Furthermore, we study the critical behaviour of the compound near T_c, which confirms the validity of the 2D XY spin model proposed in previous studies [31,32].

5.2 Experimental Details

5.2.1 Crystal Growth

An antisolvent method was used to synthesize $(PMA)_2CuCl_4$ crystals. First, the precursor salt phenylmethylammonium chloride ((PMA)Cl) was prepared. A 1:1 molar ratio of phenylmethylamine (Sigma Aldrich, for synthesis) and HCl was mixed in ethanol (1.25M, Sigma Aldrich) as a solvent and left to dry at 60 °C on a hot plate. The white powder obtained was washed three times with diethyl ether (Macron Chemicals) and vacuum dried overnight. For the growth of $(PMA)_2CuCl_4$ crystals, a 1:2 molar ratio of (PMA)Cl and anhydrous $CuCl_2$ (Alfa Aesar, 98%) was dissolved in a separate flask with methanol as the solvent. The two solutions were mixed and stirred for ~2h. A two-layer solution was then prepared by slowly adding acetonitrile (Sigma Aldrich, anhydrous 99.8%) on top of the methanol solution and was placed in a 40 °C water bath. The solution was left to evaporate for 3-4 days. We obtained two different products from the synthesis: $(PMA)_2CuCl_4$ crystals in the form of brown platelets, and dark green needles that were identified by single-crystal X-ray diffraction as an oxido-copper cluster compound, a member of the family with general formula $Cu_4OX_6(L')_4$ (X= halide, L'= ligand), in this case with X = Cl and L' = PMA [33–35].

5.2.2 X-Ray Diffraction

Single-crystal X-ray diffraction (XRD) measurements were carried out using a Bruker D8 Venture diffractometer with Mo-Kα radiation. The crystal was mounted in a fibre loop using cryo-oil. The measurement temperature was controlled by a nitrogen flow using an Oxford Cryostream Plus. Data were processed using the Bruker APEX III software. Structure solution was carried out using direct methods and refinement was performed using the SHELXTL software. In addition,

powder XRD measurement was carried out on hand-ground $(PMA)_2CuCl_4$ crystals using a Bruker D8 Advance diffractometer equipped with a Cu Kα-source.

5.2.3 Magnetic Properties Measurement

A Quantum Design MPMS SQUID magnetometer was used to carry out the magnetic measurements. Several single crystals were stacked together such that measurements were performed with the magnetic field applied in-plane. The temperature dependence of the DC magnetization was measured from 5-300K in various fields ranging from 5 Oe to 1 kOe. AC magnetization measurements were carried out from 2-25 K using an AC field of 3.8 Oe superimposed on a DC field of 200 Oe. Isothermal magnetization versus field measurements were performed from +70kOe to -70kOe at 1 K intervals between 5 and 30 K.

5.3 Results and Discussion

5.3.1 Structural Analysis

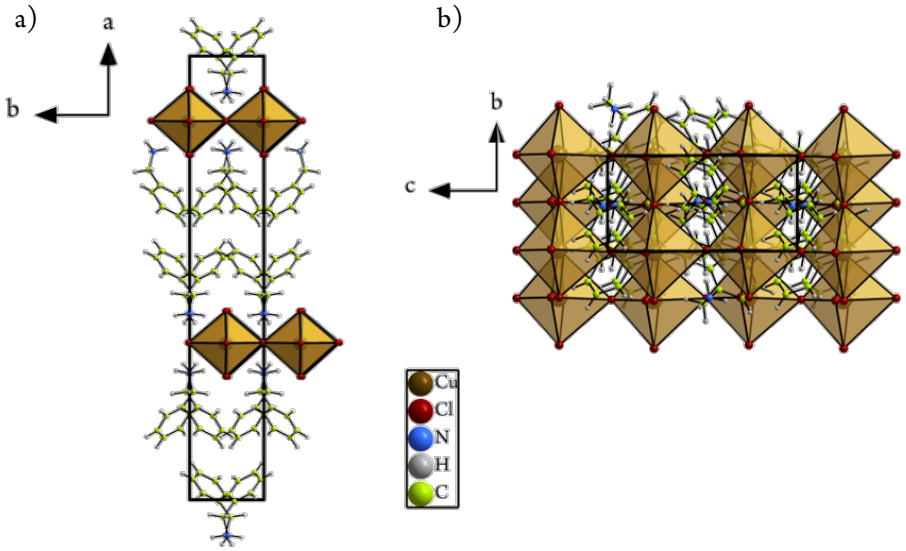

Figure 5.1 *Structure of $(PMA)_2CuCl_4$ viewed along a) c-axis and b) a-axis.*

Previous studies of $(PMA)_2CuCl_4$ based on powder XRD data reported that the crystal structure is orthorhombic at room temperature, with space group *Pbca* [28,36]. Here, our single-crystal XRD data indicate that the symmetry is monoclinic with space group Cc between 100 K and room temperature (Fig. 5.1). The associated structural parameters at 100 and 300K are presented in Table 5.1.

Reciprocal lattice images reconstructed from raw data are given in Fig. 5.2. The reflection condition for a C-centred lattice is observed: hkl, h+k = 2n. The condition h0l, l=2n is also observed and corresponds to a c-glide plane perpendicular to the b-axis. This implies the space groups C2/c or Cc, and the structure could only be solved in the latter space group. In the 0kl plane (Fig. 5.2a) many extra spots with half-integer values of k are observed, which suggests that the b-axis is doubled. However, these spots are projections of the rather diffuse, streaky rows of spots with half-integer k apparent in the hk0 projection (Fig. 5.2c). Therefore, the doubled b-axis probably corresponds to order that is rather short-range in nature. Attempts to solve the structure in an a × 2b × c unit cell were unsuccessful. The presence of this supercell implies that our solved structure should be considered an average structure only, and the rather high fit factors R1 and wR2 also suggest that the detailed structure is more complex.

Table 5.1 Structural parameters of $(PMA)_2CuCl_4$ measured at 100 K and 300 K

	100 K	300 K
Crystal system	Monoclinic	
Space group	Cc	
a (Å)	31.436(3)	31.846 (7)
b (Å)	5.2247 (5)	5.2624 (11)
c (Å)	10.4816 (12)	10.588 (2)
β (degrees)	99. 379 (7)	98.553 (9)
V (Å^3)	1698.5	1754.72
ρ (g/cm^3)	1.649	1.596
Absorption coeff. (mm^{-1})	1.91	1.85
f (000)	860	860
Index ranges	-38≤h≤38, -6≤k≤ 6, -13≤l≤ 13	-34≤h≤34, -5≤k≤5, -11≤l≤11
Goodness of fit	1.083	1.0692
R indices	wR2 = 0.2898	wR2 = 0.1887
	R1 = 0.1024	R1 = 0.0586
Largest diff. peak/hole (e/Å^3)	2.63/-2.18	1.15/-1.59

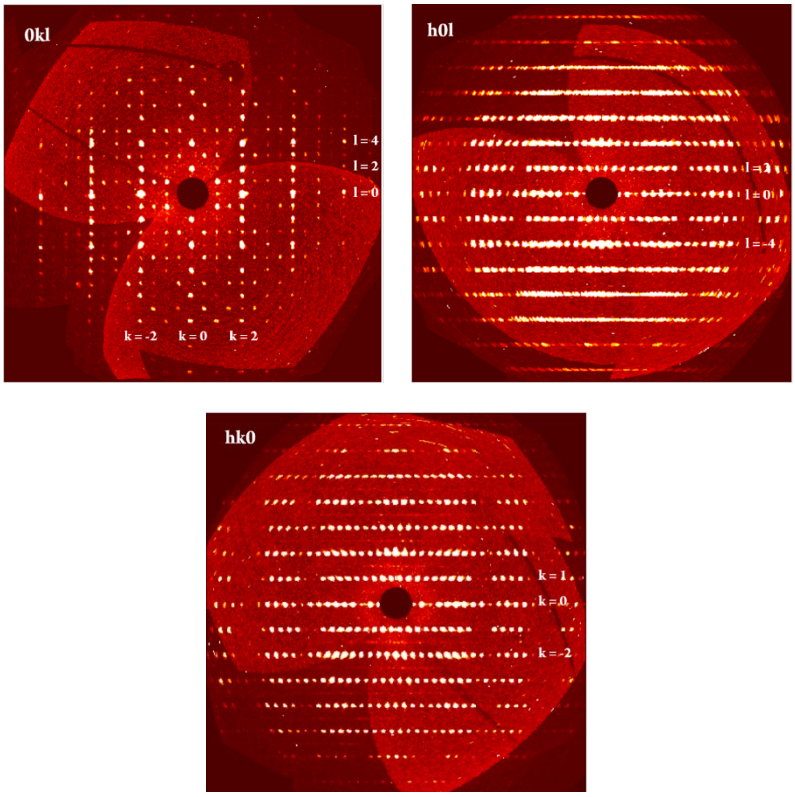

Figure 5.2 ***Reciprocal lattice images reconstructed from raw single-crystal XRD data:*** *a) (0kl), b) (h0l) and c) (hk0) projections. The (0kl) projection shows half-integer k indices, suggesting a superstructure of a × 2b × c.*

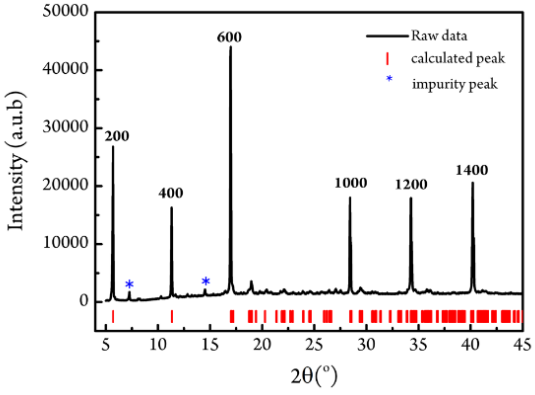

Figure 5.3 ***Room-temperature powder XRD pattern of ground $(PMA)_2CuCl_4$ crystals****. Red markers show the expected peak positions based on the structure determined by single-crystal XRD and the blue asterisks indicate peaks from the main impurity phase (oxido-Cu cluster compound).*

We also carried out powder XRD on a sample comprised of crushed crystals, as shown in Fig. 5.3. The allowed peak positions associated with the single-crystal XRD structure are indicated and match well with the measured peaks. The pattern shows a strong preferred orientation along the layer stacking direction [h00] due to the plate-like morphology of the crystals, manifested by a high intensity on the corresponding peaks. Impurity peaks are observed, especially below $2\theta = 15°$, and correspond to the oxido-copper cluster compound mentioned above.

5.3.2 Magnetic Properties

The temperature dependent DC magnetization of $(PMA)_2CuCl_4$ was measured in field-cooled mode from 5-300 K with an in-plane external magnetic field of 200 Oe or 1 kOe (Fig. 5.4a). The sudden increase in magnetization below ~10 K suggests the onset of ferromagnetic ordering. This is supported by the S-shaped magnetization versus applied field curve (Fig. 5.4b). No hysteresis is observed. The transition temperature, T_c, is in the range 9-10 K depending on the magnitude of the external magnetic field applied up to 1 kOe, as determined from the sharp peak in the differential magnetization curve in the inset of Fig. 5.4a. Fig. 5.5 shows the AC magnetization as a function of temperature, where a frequency-independent peak at 9.5 K is observed in the real component χ' when measured in an underlying DC field of 200 Oe, which agrees with the DC magnetization in Fig. 5.3a. A corresponding peak is also present in the imaginary part χ'' of the AC magnetization; such a peak is related to irreversible magnetization processes and is consistent with ferromagnetic ordering involving the rearrangement of domain walls.

Curie-Weiss fitting to the inverse DC susceptibility data in the temperature range above 150K (Fig. 5.6) yields a positive Curie-Weiss temperature (θ_{CW}) of 71.7K. This large, positive value of θ_{CW} compared to the 3D ordering temperature T_c shows that in-plane 2D ferromagnetic interactions are strong. The effective magnetic moment is determined as $\mu_{eff} = 1.44\ \mu_B$, which is slightly smaller than the theoretical spin-only value for Cu^{2+} of 1.73 μ_B. We note that the curve is not perfectly linear over the temperature range measured.

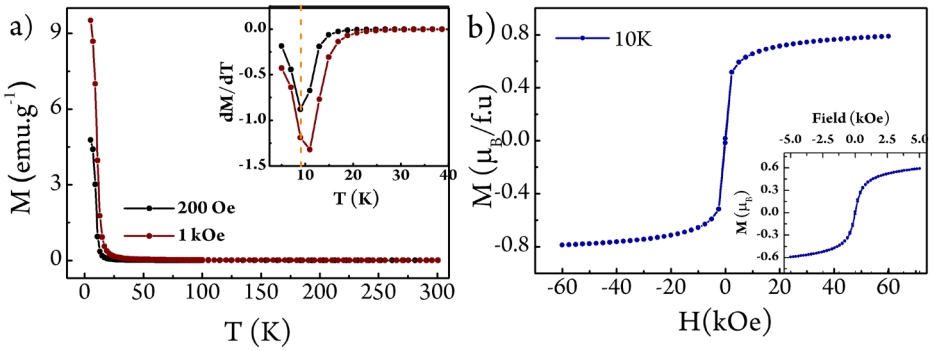

Figure 5.4 *a) Temperature dependence of field-cooled in-plane magnetization of $(PMA)_2CuCl_4$. b) Field dependent magnetization at 10K; the inset shows the low-field region.*

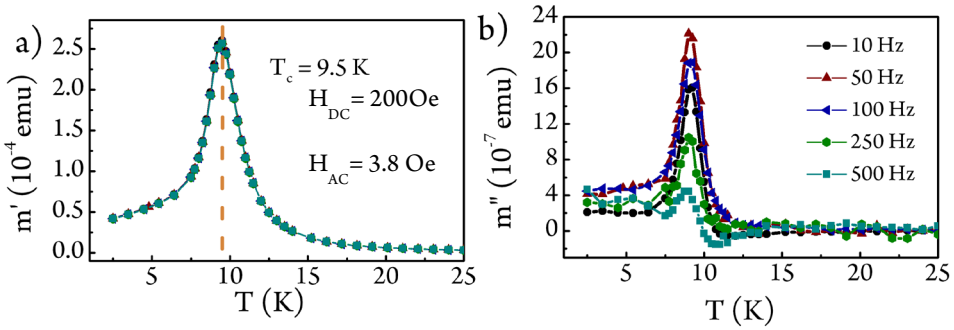

Figure 5.5 *Temperature dependent AC magnetization of stacked $(PMA)_2CuCl_4$ crystals: a) real part and b) imaginary part. The real component of the AC susceptibility shows a peak at 9.5 K which is consistent with the peak observed in the DC susceptibility and indicates the Curie temperature.*

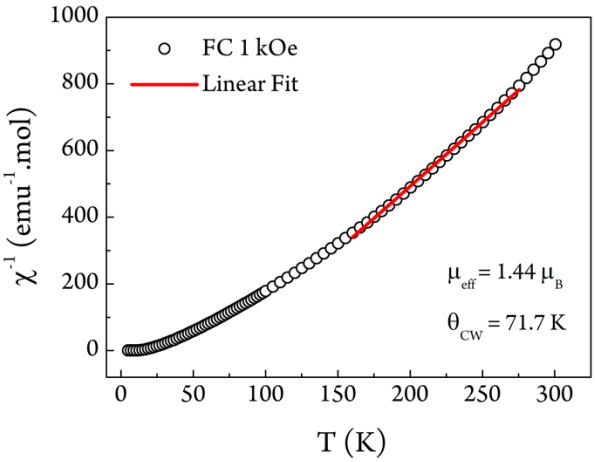

Figure 5.6 *Curie-Weiss fit to inverse field-cooled magnetic susceptibility of stacked $(PMA)_2CuCl_4$ crystals. The black circles indicate the inverse susceptibility data of $(PMA)_2CuCl_4$ and the red line is a linear fit to the data in the temperature range 150-280 K.*

5.3.3 Magnetocaloric Effect

The field-dependence of T_c that is apparent in Fig. 5.4a suggests the presence of a significant magnetic entropy change at the onset of ferromagnetic ordering. This shift in T_c is more obvious in Fig. 5.7, where the temperature dependent magnetization is plotted for lower applied fields of 5-200 Oe.

In addition to a large magnetic entropy change, good magnetocaloric materials exhibit minimal losses on cycling the temperature or magnetic field, thus a second-order magnetic phase transition is desirable. As shown by the field-dependent magnetization in Fig. 5.4b we do not observe any hysteresis, which suggests a second-order nature. The order of the magnetic phase transition can be probed using an Arrot plot, which shows the relation between the square of the magnetization (M^2) and H/M obtained from a series of isothermal magnetization versus field measurements, as shown in Fig. 5.8b [37]. According to the Banerjee criterion, a positive slope is obtained for materials that exhibit a second-order phase transition, while a negative slope corresponds to a first-order transition [38]. Our plots exhibit positive slopes for the temperature range from 5-30 K, which suggests a second-order phase transition.

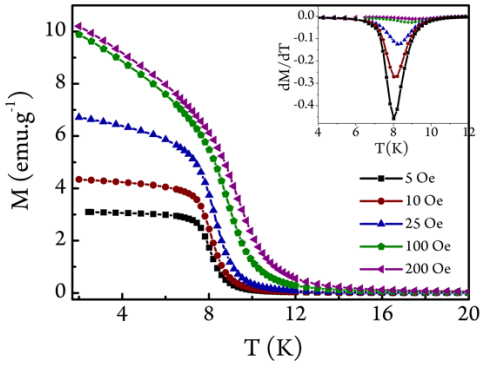

Figure 5.7 *Magnetization versus temperature measured in low applied fields; the inset shows the derivative dM/dT versus temperature.*

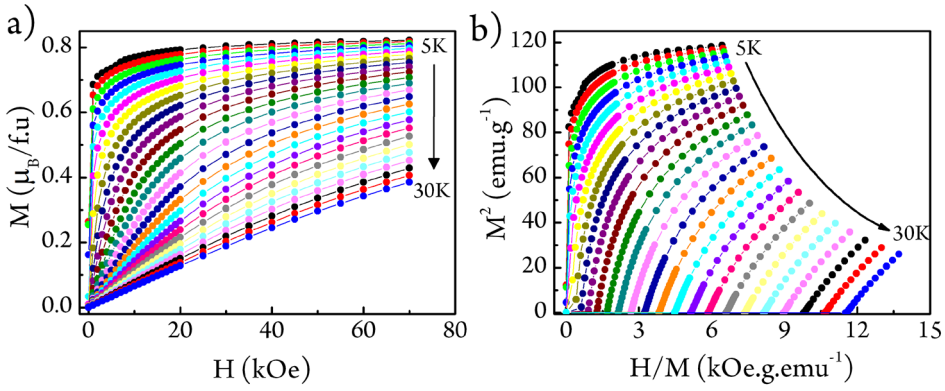

Figure 5.8 *a) Isothermal magnetization versus applied field curves measured at temperatures from 5-30K. b) Corresponding Arrot plot, suggesting a second-order magnetic phase transition.*

Isothermal magnetization versus applied field data also allow us to calculate the magnetic entropy changes that arise due to the applied field. Field-dependent magnetization measurements were carried out in the range 0-70 kOe at constant temperatures from 5-30 K (shown in Fig. 5.8a). By using Maxwell's equation, the entropy change ΔS can be calculated as [20]:

$$\left(\frac{\partial S}{\partial T}\right)_T = \left(\frac{\partial M}{\partial T}\right)_H \tag{5.1}$$

$$\Delta S\,(T,H) = \int_0^H \left(\frac{\partial M}{\partial T}\right)_H dH \tag{5.2}$$

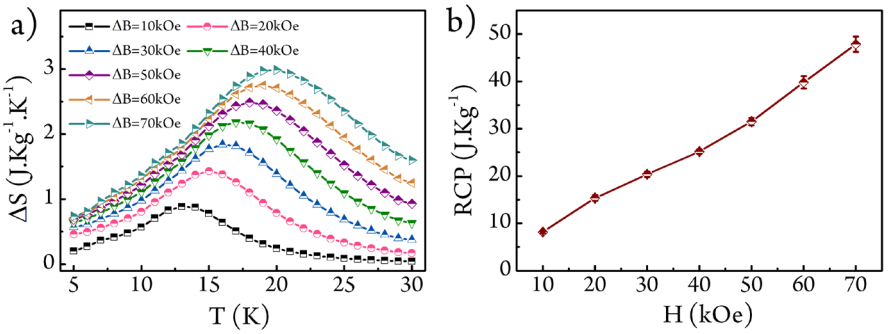

Figure 5.9 *a) Magnetic entropy change as a function of temperature at different applied fields. b) Relative cooling power (RCP) as a function of applied magnetic field.*

The magnetic entropy change plot in Fig. 5.9a exhibits a series of maxima that shift to higher temperatures as the magnetic field is increased, due to enhancement of the ferromagnetic interactions. The maximum entropy change, ΔS_M, ranges from 0.88 J/kg.K to 2.98 J/kg.K for applied fields increasing from 10 kOe to 70 kOe, respectively.

The performance of a magnetocaloric material as a coolant is often quantified by the relative cooling power (RCP), which is the ability to interchange heat between a cold and hot region in one ideal refrigeration cycle and is given by[20],

$$RCP = |\Delta S_M^{Max}| \; x \; \delta T_{FWHM} \qquad (5.3)$$

Here δT_{FWHM} is the full-width at half maximum of the magnetic entropy change curve, which was determined from Gaussian fits to the curves in Fig. 5.9a. We obtained RCP values of up to 47.8 J/Kg at 70 kOe, the highest magnetic field applied.

In table 5.2 we compare the ΔS_M value of our compound at 70 kOe to other 2D perovskites in which the magnetocaloric properties have been investigated. Based on the limited evidence of only three other reports [17–19], it is possible that the value of ΔS_M increases for smaller interlayer spacing (using shorter organic cations such as CH_3NH_3 or $C_2H_5NH_3$), but further investigations are necessary to confirm this trend. The significantly larger ΔS_M reported for $(C_2H_5NH_3)_2CoCl_4$ is likely due to the larger spin of Co^{2+} (S = 3/2) compared to Cu^{2+} (S = ½).

Table 5.2 Magnetic entropy change (ΔS_M) of $(PMA)_2CuCl_4$ in 70 kOe applied field compared to other compounds with similar Tc.

Compound	T_c (K)	ΔS_M (J/kg.K)
$(C_6H_5CH_2NH)_2CuCl_4$ (our work)	9.5	2.98 (7 T)
$(CH_3NH_3)_2CuCl_4$[17]	8.9	4.98 (5 T)
$(C_{12}H_{25}NH_3)_2CuCl_4$[18]	13	1.9 (5 T)
$(C_2H_5NH_3)_2CoCl_4$[19]	2	14.5 (7 T)

Although the magnetocaloric properties of $(PMA)_2CuCl_4$ have not previously been studied, a recent report focused on magnetodielectric (MD) coupling in the same compound [36]. It was proposed that the MD coupling is associated with a change from antiferromagnetic to ferromagnetic interlayer coupling as the magnitude of the external field is increased above ~1 kOe. Similar to our current study, a magnetic moment of ~0.5 μ_B / f.u. was measured in an applied field of 3 kOe at 12 K, implying a considerable shift in T_C with field. Other Cu- and Mn-based 2D hybrid perovskites containing arylamine-based organic cations are also known to show magnetic field-induced spin reorientations [8,11] below T_C or T_N. The weak interlayer coupling and soft ferromagnetism in the case of Cu-based 2D perovskites allow the reorientation of spins by relatively low fields, thus resulting in large magnetic entropy changes.

5.3.4. Critical Behaviour

The critical behaviour of a magnetic material near the Curie temperature associated with a second-order transition can be characterized by a series of critical exponents according to the universal scaling hypothesis. These critical exponents β, γ, and δ can be determined from the spontaneous magnetization $M_s(T)$, initial susceptibility $\chi_o(T)$, and magnetization M(H). The definitions of these exponents are as follows [39,40]:

$$M_s(T) = M_0(-\varepsilon)^{\beta},\ \varepsilon < 0, T < T_c \tag{5.4}$$

$$\chi_0{}^{-1} = \frac{h_0}{m_0}\varepsilon^{\gamma},\ \varepsilon > 0, T > T_c \tag{5.5}$$

$$M = DH^{1/\delta},\ \varepsilon = 0, T = T_c \tag{5.6}$$

Here $\varepsilon = (T-T_c/T_c)$ is the reduced temperature, while M_0, h_0/m_0, and D are the critical amplitudes. Furthermore, using the scaling hypothesis, the relationship between the variables can be expressed as

$$M(H,\varepsilon) = \varepsilon_f^{\beta} \pm (H/\varepsilon^{\beta+\gamma}) \quad (5.7)$$

where the two terms are added for $T>T_c$ and subtracted for $T<T_c$. The renormalized magnetization $m \equiv \varepsilon^{-\beta} M(H,\varepsilon)$ and the renormalized field $h \equiv \varepsilon^{-(\beta+\gamma)} H$ should follow two universal rules that differentiate the behaviour where $T<T_c$ and $T>T_c$.

Generally, Arrot plot analysis can be used to obtain the critical exponents and critical temperature. The Arrot plot presumes that the critical exponents follow mean-field theory where $\beta = 0.5$ and $\gamma = 1.0$, such that the M^2 vs H/M plots should consist of a set of a parallel straight lines. The plot corresponding to the critical temperature T_c should then pass through the origin. The intercepts with the M^2 axis and the H/M axis at any particular temperature should give the spontaneous magnetization $M_s(T)$ and initial susceptibility $\chi_o(T)$, respectively. As shown in Fig. 5.8b, the Arrot plot does not consist of straight lines, which indicates that mean-field theory is not valid for our system.

A modified Arrot plot was then used to estimate the critical exponents of $(PMA)_2CuCl_4$. A set of known critical exponents from different models were used. The modified Arrot plot was constructed using the Arrot-Noakes equation of state [41]:

$$(H/M)^{1/\gamma} = a\left(\frac{T-T_c}{T_c}\right) + b\,M^{1/\beta} \quad (5.8)$$

Here the parameters *a* and *b* are considered constant. The plot of $(H/M)^{1/\gamma}$ vs $M^{1/\beta}$ should consist of a set of parallel straight lines if the correct set of critical exponents are chosen. Fig. 5.10 presents modified Arrot plots for several 3D models: the 3D Heisenberg, 3D XY, 3D Ising, and tricritical mean-field model [42,43]. None of the plots consist of parallel straight lines, which implies that the 3D models are invalid. This observation is not unexpected, as it is known that $(PMA)_2CuCl_4$ possesses 2D characteristics. Therefore, we next used critical exponents that were previously determined for the 2D Ising model [44]; the corresponding plot is shown in Fig. 5.11a. In contrast to the 3D models, the 2D Ising model yields a set of curves that are almost linear, consistent with 2D characteristics.

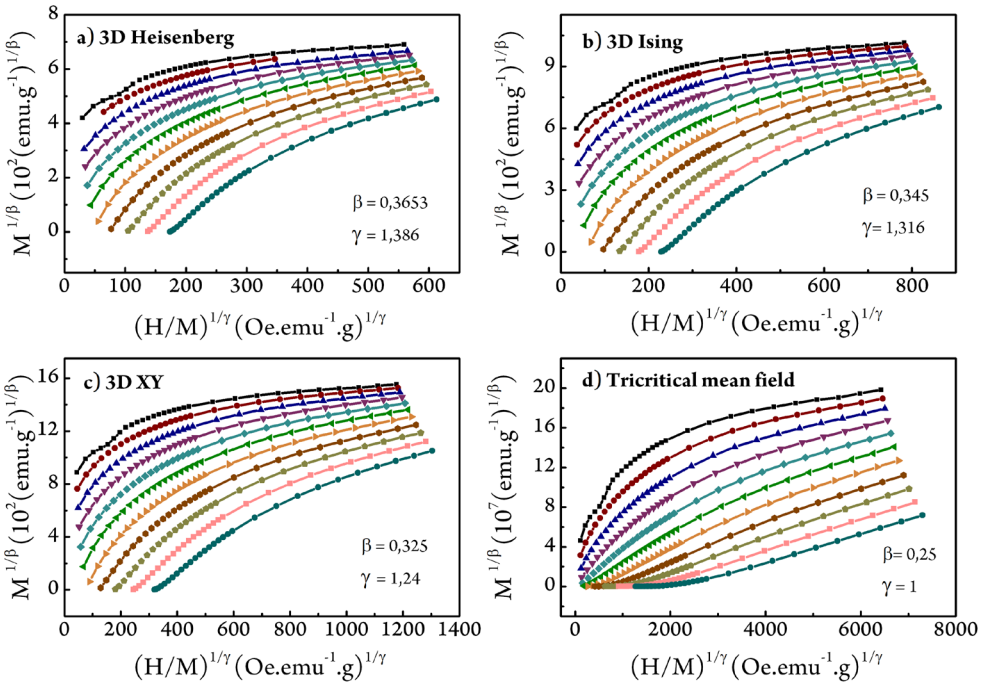

***Figure 5.10* Modified Arrot-Noakes plots for $(PMA)_2CuCl_4$ crystals.** *The plots constructed using various 3D models (a,b,c) and tricritical mean field model (d). None of the curves are linear, which indicates that the 3D model is invalid for our system.*

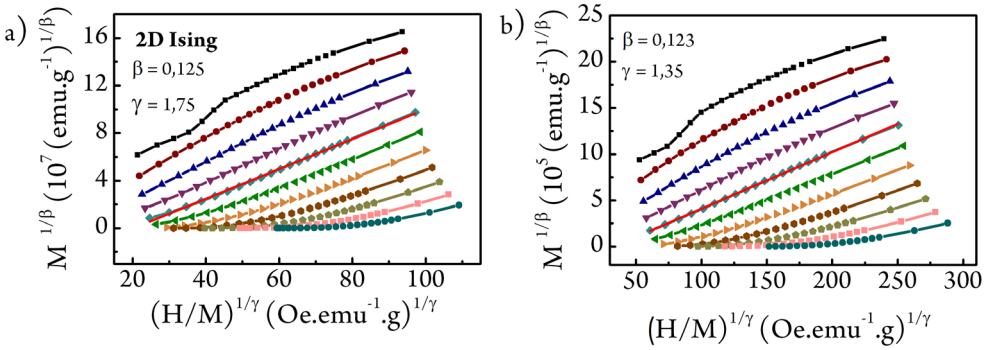

Figure 5.11 *Modified Arrot-Noakes plots for a) 2D Ising model and b) with γ and β values obtained from the critical isotherm approximation presented in Eq. (5.6) and (5.9).*

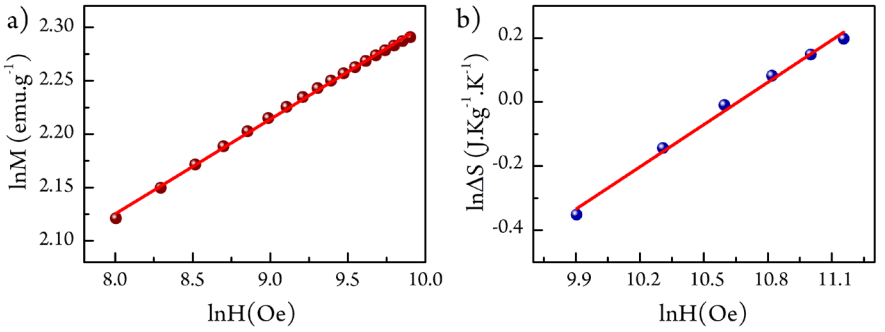

Figure 5.12 *a) Magnetization vs applied field on a log-log scale measured at T_c; the solid line is a linear fit to Eq. (5.6). b) Field dependence of magnetic entropy change at T_c on a log-log scale; the solid line represents a linear fit to Eq. (5.8).*

To estimate the critical exponents of our system, we first used the critical isotherm approximation as stated in Eq. (5.6) to obtain δ. We plotted ln(M) vs ln(H); the slope of this graph gives us 1/δ. To obtain the β exponent the field dependence of the magnetic entropy change can be used, as stated in the equation below [40,45,46]:

$$\Delta S_{m|T=T_c} \propto H^n; \ldots\ldots n = 1 + \frac{1}{\delta}\left(1 - \frac{1}{\beta}\right) \qquad (5.9)$$

A plot of ΔS_m versus H on a log-log scale should be linear, where the slope gives the value of n. The two plots are presented in Fig. 5.12a and b, respectively. Since δ is obtained from Fig. 5.12a, the value of β can be extracted from Fig. 5.12b. The γ exponent can then be calculated by Widom scaling where $\delta = 1 + \gamma/\beta$ [47].

Finally, we constructed a modified Arrot-Noakes plot using the extracted critical exponents, shown in Fig. 5.11b. The curves are close to linear at temperatures around T_c, and the plot corresponding to T_c intercepts the origin. The values of exponents β=0.123 and γ=1.35 are close to those for the known 2D Ising model (β=0.125 and γ=1.75) [44]. Previously, Kosterlitz found that the critical exponents for the 2D XY and 2D Ising models are similar [48]. Since $(PMA)_2CuCl_4$ has previously been described as a 2D XY magnet, our results are consistent with these findings.

The reliability of the critical exponents can be tested using Eq. (5.4), such that the renormalized magnetization vs renormalized field graph should show different behaviour below and above T_c. This is indeed the case as shown in Fig. 5.13 where a splitting of the curves is observed in the low field region. The inset of Fig. 5.13 shows the same plot on a log-log scale, where the splitting is more pronounced.

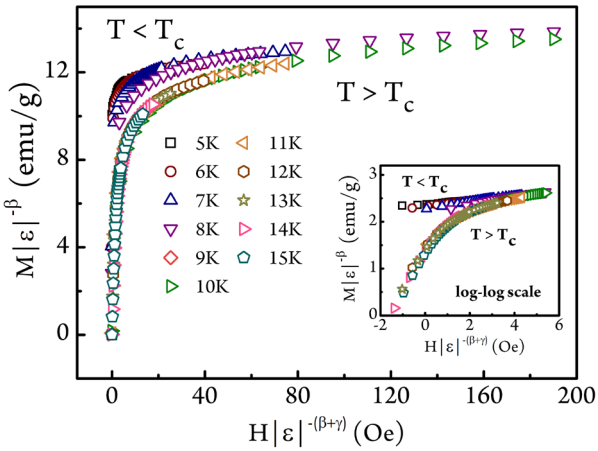

Figure 5.13 *Logarithmic scaling plot used to check the reliability of the critical exponents obtained, showing two different trends for T<Tc and T>Tc.*

5.4 Conclusions

We have restudied the crystal structure of $(PMA)_2CuCl_4$ and find that it crystallizes in the monoclinic, non-centrosymmetric space group Cc instead of the previously reported orthorhombic *Pbca* structure. Magnetization measurements show ferromagnetic ordering below T_c = 9.5K, in agreement with previous reports. We demonstrate a large magnetocaloric effect by determining a magnetic entropy change, ΔS_M, that ranges from 0.88 J/kg.K to 2.98 J/kg.K for fields of 10kOe to 70kOe, respectively. The corresponding relative cooling power reaches a maximum of 47.8 J/Kg in a field of 70 kOe. The large magnetic entropy change in $(PMA)_2CuCl_4$ indicates the potential of layered organic-inorganic perovskites for use in solid-state cooling devices. We have also investigated the behaviour of $(PMA)_2CuCl_4$ in the vicinity of T_c by determining the critical exponents using the critical isotherm approximation. Values of $\gamma = 1.45$, $\beta = 0.123$, and $\delta = 12.76$ are obtained, which are consistent with critical exponents expected for the 2D XY model.

5.5 References

1 L. Pedesseau, D. Sapori, B. Traore, R. Robles, H. H. Fang, M. A. Loi, H. Tsai, W. Nie, J. C. Blancon, A. Neukirch, S. Tretiak, A. D. Mohite, C. Katan, J. Even and M. Kepenekian, *ACS Nano*, 2016, **10**, 9776–9786.

2 M. D. Smith, B. A. Connor and H. I. Karunadasa, *Chem. Rev.*, 2019, **119**, 3104–3139.

3 T. D. Huan, V. N. Tuoc and N. V. Minh, *Phys. Rev. B*, 2016, **93**, 094105.

4 M. D. Smith, E. J. Crace, A. Jaffe and H. I. Karunadasa, *Annu. Rev. Mater. Res.*, 2018, **48**, 111–136.

5 Z. Cheng and J. Lin, *CrystEngComm*, 2010, **12**, 2646–2662.

6 N. A. Benedek, J. M. Rondinelli, H. Djani, P. Ghosez and P. Lightfoot, *Dalt. Trans.*, 2015, **44**, 10543–10558.

7 L. Mao, C. C. Stoumpos and M. G. Kanatzidis, *J. Am. Chem. Soc.*, 2019, **141**, 1171–1190.

8 S.-H. Park, I.-H. Oh, S. Park, Y. Park, J. H. Kim and Y.-D. Huh, *Dalt. Trans.*, 2012, **41**, 1237–1242.

9 G. Park, I. H. Oh, J. M. S. Park, J. Jung, C. Y. You, J. S. Kim, Y. Kim, J. H. Jung, N. Hur, Y. Kim, J. Y. Kim, C. S. Hong and K. Y. Kim, *Sci. Rep.*, 2018, **8**, 4661.

10 S. Y. Kim, J. M. Yang, E. S. Choi and N. G. Park, *Adv. Funct. Mater.*, 2020, **30**, 2002653.

11 B. Huang, J. Y. Zhang, R. K. Huang, M. K. Chen, W. Xue, W. X. Zhang, M. H. Zeng and X. M. Chen, *Chem. Sci.*, 2018, **9**, 7413–7418.

12 A. A. Nugroho, Z. Hu, C. Y. Kuo, M. W. Haverkort, T. W. Pi, D. Onggo, M. Valldor and L. H. Tjeng, *Phys. Rev. B*, 2016, **94**, 184404.

13 M. E. Kamminga, R. Hidayat, J. Baas, G. R. Blake and T. T. M. Palstra, *APL Mater.*, 2018, **6**, 066106.

14 L. Zou, H. X. Liu, L. L. Guo, G. T. Xu and G. F. Xue, *Adv. Mater. Res.*, 2011, **311**–**313**, 2146–2150.

15 P. Zhou, J. E. Drumheller, B. Patyal and R. D. Willett, *Phys. Rev. B*, 1992, **45**, 12365–12376.

16 M. I. Asghar, J. Zhang, H. Wang and P. D. Lund, *Renew. Sustain. Energy Rev.*, 2017, **77**, 131–146.

17 Y. Ma, K. Zhai, L. Yan, Y. Chai, D. Shang and Y. Sun, *Chinese Phys. B*, 2018, **27**, 027501.

18 M. Bochalya and S. Kumar, *J. Appl. Phys.*, 2020, **127**, 055501.

19 A. Sen, S. Roy, S. C. Peter, A. Paul, U. V. Waghmare and A. Sundaresan, *J. Solid State Chem.*, 2018, **258**, 431–440.

20 A. Gschneidner, V. K. Pecharsky and A. O. Tsokol, *Reports Prog. Phys.*, 2005, **68**, 1479–1539.

21 V. K. Pecharsky and K. A. Gschneidner, *J. Magn. Magn. Mater.*, 1999, **200**, 44–56.

22 V. Zverev and A. M. Tishin, *Magnetocaloric Effect: From Theory to Practice*, Elsevier Ltd., 2016.

23 K. A. Gschneidner and V. K. Pecharsky, *Int. J. Refrig.*, 2008, **31**, 945–961.

24 K. G. Sandeman, *Scr. Mater.*, 2012, **67**, 566–571.

25 S. Shahrokhi, W. Gao, Y. Wang, P. R. Anandan, M. Z. Rahaman, S. Singh, D. Wang, C. Cazorla, G. Yuan, J. M. Liu and T. Wu, *Small Methods*, 2020, **4**, 2000149.

26 A. O. Polyakov, A. H. Arkenbout, J. Baas, G. R. Blake, A. Meetsma, A. Caretta, P. H. M. Van Loosdrecht and T. T. M. Palstra, *Chem. Mater.*, 2012, 24, 133–139.

27 G. Park, I. H. Oh, J. M. S. Park, S. H. Park, C. S. Hong and K. S. Lee, *Phys. B Condens. Matter*, 2018,

551, 89–93.

28 A. Dupas, K. Le Dang, J. P. Renard and P. Veillet, *J. Chem. Phys.*, 1976, **65**, 3–7.

29 Y. Kimishima, *J. Magn. Magn. Mater.*, 1990, **90–91**, 301–302.

30 W. E. Estes, D. Bruce Losee and W. E. Hatfield, *J. Chem. Phys.*, 1980, **72**, 630–638.

31 Y. Kimishima, *Jpn. J. Appl. Phys.*, 1987, **26**, 867–868.

32 H. Han, L. Zhang, X. Zhu, H. Du, M. Ge, L. Ling, L. Pi, C. Zhang and Y. Zhang, *Sci. Rep.*, 2016, **6**, 39338.

33 S. Becker, M. Dürr, A. Miska, J. Becker, C. Gawlig, U. Behrens, I. Ivanović-Burmazović and S. Schindler, *Inorg. Chem.*, 2016, **55**, 3759–3766.

34 S. Becker, U. Behrens and S. Schindler, *Eur. J. Inorg. Chem.*, 2015, **2015**, 2437–2447.

35 S. Löw, J. Becker, C. Würtele, A. Miska, C. Kleeberg, U. Behrens, O. Walter and S. Schindler, *Chem. Eur. J.*, 2013, **19**, 5342–5351.

36 Y. H. Kim and N. Hur, *J. Korean Phys. Soc.*, 2020, **77**, 1026–1030.

37 A. Arrott, *Phys. Rev.*, 1957, **108**, 1394–1396.

38 S. K. Banerjee, *Phys. Lett.*, 1964, **12**, 16–17.

39 H. E. Stanley, *Rev. Mod. Phys.*, 1999, **71**, 358–366.

40 R. Pełka, P. Konieczny, M. Fitta, M. Czapla, P. M. Zieliński, M. Bałanda, T. Wasiutyński, Y. Miyazaki, A. Inaba, D. Pinkowicz and B. Sieklucka, *Acta Phys. Pol. A*, 2013, **124**, 977–988.

41 A. Arrott and J. E. Noakes, *Phys. Rev. Lett.*, 1967, **19**, 1–4.

42 S. N. Kaul, *J. Magn. Magn. Mater.*, 1985, **53**, 5–53.

43 K. Huang, *Statistical Mechanics 2nd ed.*, Wiley, New York, 1987.

44 J. C. Le Guillou, *Phys. Rev. B*, 1980, **21**, 3976–3998.

45 A. Tekgül, Çaklr, M. Acet, M. Farle and N. Ünal, *J. Appl. Phys.*, 2015, **118**, 153903.

46 J. Fan, L. Pi, L. Zhang, W. Tong, L. Ling, B. Hong, Y. Shi, W. Zhang, D. Lu and Y. Zhang, *Appl. Phys. Lett.*, 2011, **98**, 300–303.

47 B. Widom, *J. Chem. Phys.*, 1965, **43**, 3898–3905.

48 J. M. Kosterlitz, *J. Phys. C Solid State Phys.*, 1974, **7**, 1046–1060.